Available online at www.sciencedirect.com
SCIENCE DIRECT®
Pergamon
Acta Materialia 51 (2003) 3663–3674
Acta MATERIALIA
www.actamat-journals.com

# Distribution of grain boundaries in magnesia as a function of five macroscopic parameters

David M. Saylor [1], Adam Morawiec [2], Gregory S. Rohrer *

*Carnegie Mellon University, Materials Science and Engineering Department, Pittsburgh, PA 15213-3890, USA*

Received 2 December 2002; received in revised form 21 March 2003; accepted 21 March 2003

**Abstract**

A semi-automated method has been used to measure all five macroscopically observable parameters of $4.1 \times 10^6$ boundary plane segments making up 5.4 $mm^2$ of boundary area in a hot-pressed magnesia polycrystal. The observations allow a complete description of the distribution of crystal orientations, grain boundary misorientations, and the crystallographic orientations of grain boundary planes. Among the low misorientation angle grain boundaries, there is a preference for tilt boundaries, especially those with boundary plane normals in the <110> direction. At all fixed misorientations, there is a preference for boundaries with a boundary plane normal in the <100> direction. These boundaries are generally asymmetric and occur at least twice as frequently as the average boundary for each fixed misorientation.


*Keywords:* Grain boundaries; Ceramics; Microstructure; Electron backscattering patterns (EBSP); Texture

## 1. Introduction

The principal challenge associated with characterizing grain boundary networks in real polycrystals is that the number of physically distinct interfaces is very large. Distinct grain boundaries in a material with a centrosymmetric crystal structure are specified by five macroscopic and three microscopic parameters [1]. The macroscopic degrees of freedom can be parameterized by three rotation angles that bring two misoriented crystals into coincidence, and two spherical angles that specify the orientation of the boundary plane [2]. The three microscopic degrees of freedom are the components of a translation vector that defines the relative positions of two adjacent crystals. Using the methods described here, it is not possible to resolve the microscopic parameters and we therefore assume that if two grain boundaries in the same polycrystal have the same five macroscopically observable parameters, then they are identical and have the same properties. The neglect of these parameters is justified if, over time, macroscopically indistinguishable boundaries experience the same range of microscopic configurations and, therefore, have the same average observable

* Corresponding author. Tel.: +1-412-268-2696; fax: +1-412-268-3113.
*E-mail address:* gr20@andrew.cmu.edu (G.S. Rohrer).
[1] Current address: National Institute of Standards and Technology, Gaithersburg, MD, USA
[2] Current address: Institute of Metallurgy and Materials Science, Polish Academy of Sciences, Cracow, Poland

1359-6454/03/$30.00 
doi:10.1016/S1359-6454(03)00181-2

properties. Considering only the macroscopic parameters, and assuming that they can be resolved with 5° of resolution, then there are approximately $10^5$ possible different boundaries between cubic crystals [3].

The most extensive studies of grain boundary distributions have been carried out over the three misorientation parameters using X-ray diffraction techniques, which are generally insensitive to the grain boundary plane orientation [4,5]. The three-dimensional structure of the interfacial network can be determined by stereoscopic microradiagraphy [6] or by serial sectioning and the microscopic analysis of section planes [7], but orientation measurements are required [8] to recover the crystallographic information. All five macroscopic parameters can be simultaneously measured by transmitted light microscopy using a polarizing microscope equipped with a universal stage [9], transmission electron microscopy [10], or three-dimensional X-ray diffraction microscopy [11]. However, these techniques have not yet been capable of producing the number of measurements required to reliably sample the complete range of distinguishable grain boundaries. Therefore, we do not yet know if all the geometric possibilities are realized in polycrystals or how the relative frequency of occurrence of different types of boundaries varies in polycrystals of different materials.

The purpose of the present paper is to describe the frequency with which different types of grain boundaries occur in a MgO polycrystal that we have examined using a combination of orientation imaging [12], secondary electron imaging, and serial sectioning. A summary of these findings has recently been presented in a brief communication [13]. The present paper is meant to provide the details of the experimental methods and the observed distribution. In a companion paper, we describe relative grain boundary energies derived from our observations and the origin of the observed grain boundary plane texture [14] that arises during grain growth.

## 2. Experimental method

### 2.1. Approach

To characterize the geometry and crystallography of large quantities of contiguous crystallites, we have used an automated scanning electron microscope (SEM) mapping system to control both the stage and beam position and to record images and electron backscattered diffraction patterns (EBSPs). To determine the details of the grain boundary geometry, secondary electron images are recorded with submicron resolution. After the image is recorded, EBSP measurements are made at regular intervals within the field of view, referred to as a sector. The process is carried out under computer control so that when one sector is characterized, the microscope stage is automatically moved to an adjacent sector and the process is repeated. Because we use SEM images to determine grain boundary positions, the orientation measurements can be conducted at relatively coarse intervals. Thus, compared to the conventional automated EBSP-based mapping methods, we are able to resolve the boundary positions accurately without accumulating redundant orientation data [12]. After a surface is mapped, high precision serial sectioning is used to remove a thin layer and the process is repeated. These data allow us to reconstruct the three-dimensional grain boundary network and specify the misorienation ($\Delta g$) and the boundary normal direction ($\mathbf{n}$) for a large number of planar segments. The quantity we refer to as the grain boundary distribution, $\lambda(\Delta g,\mathbf{n})$, is the frequency of occurrence of a specific type of grain boundary, distinguished on the basis of $\Delta g$ and $\mathbf{n}$, in units of multiples of a random distribution (MRD).

### 2.2. Data acquisition

The automated mapping system described above was integrated with a Phillips XL40 FEG SEM. The MgO sample ($Fm\bar{3}m$, rock salt structure) examined here was originally prepared for a study of the surface energy anisotropy and the details of the preparation can be found in an earlier publication describing those results [15]. Briefly, the

sample was hot pressed at 1700 °C for 1 h, annealed in air for 48 h at 1600 °C, and had an average grain size of 109 μm. To reveal the positions of the grain boundaries, the sample was thermally etched at 1400 °C for 5 h in air. During this treatment, grooves approximately 2 μm wide formed at the boundaries; there was no evidence for grain boundary migration during this treatment. A thin carbon coating was then applied to eliminate charging in the SEM. All of the images and EBSPs were recorded with the sample tilted at an angle of 60° with respect to the beam. On each layer, three scan areas, each consisting of a 14 × 14 grid of sectors were characterized. In each of the 196 sectors in each area, a tilt-corrected image at 750× magnification and 300 uniformly distributed EBSPs were recorded. The pixel-to-pixel resolution in the SEM image was 0.25 μm and the spacing between adjacent EBSP measurements was approximately 8 μm. The EBSP patterns were indexed using an algorithm previously described by Morawiec [16], which returns a rotation relating the sample reference frame to the crystal reference frame [17].

After scanning was completed on each layer, approximately 7 μm of material was removed ($\Delta h$) and the entire process was repeated. Serial sectioning was accomplished using an automatic polisher (Logitech PM5) capable of preparing very flat and parallel surfaces. Polishing was carried out using an alkaline (pH ~10) colloidal silica (0.05 μm) slurry. The amount of material removed and the surface flatness was measured using an inductive axial movement gauge head with a resolution of 0.1 μm (Brown and Sharpe, TESR, model TT22); surfaces were determined to be flat within ±0.3 μm over lateral dimensions of 1 cm. On each layer, each of the three scan areas (each consisting of a 14 × 14 sectors) were visually aligned to cover the same area as the corresponding scans on the previous layer. This was repeated until data from three to five layers were accumulated for each scan area and approximately 0.15 $mm^3$ volume of material had been characterized.

### 2.3. Reconstruction of the grain boundary network

Because the amount of material removed between section planes ($\Delta h$ ~7 μm) was small compared to the grain size (109 μm), it is possible to reconstruct the geometric configuration of the characterized volume of microstructure in the following way. First, the geometry of the crystallites in each section plane was extracted from the SEM images. Next, using the coarse map of orientations derived from the EBSP measurements, orientations were assigned to each crystallite on the section plane. After the geometry and orientation of all grains on corresponding section planes were determined, the adjacent planes were aligned to establish the connectivity of the grains between the section planes. Finally, a meshed surface representing the grain boundaries between adjacent section planes was created. From the meshed boundary surface, all five macroscopic parameters for each element in the mesh could be specified. The procedures used for this analysis are described in more detail in the remainder of this subsection.

The initial step in the volume reconstruction procedure is to extract the geometry of the crystallites on each characterized layer. This involves transforming the grayscale secondary electron images to spatially correct, binary images of the grain boundary skeleton. Although the recorded images were initially tilt-corrected by the software in the SEM, substantial geometric distortions still arise. These distortions were characterized using a lithographically produced standard grating with known dimensions and the images were corrected using an algorithm described by Kapur and Casasent [18]. To accurately specify the crystallite geometry in each image, the grain boundaries were manually digitized using a program that allows the operator to trace the boundary with a computer mouse. In this process, the two-dimensional grain boundary network is approximated as a skeleton made up of straight line segments. This skeletonization process is illustrated schematically in Fig. 1.

To combine the 196 skeletonized images in each 14 × 14 scan area in a single reference frame, we must first establish the relative positions of each of the sectors with greater accuracy than the positions provided by the microscope's stage coordinates. This is possible because adjacent images in each planar section are deliberately recorded so that all adjacent sectors overlap. By maximizing the contrast correlation in the overlapped region, it is possible to determine an offset between each

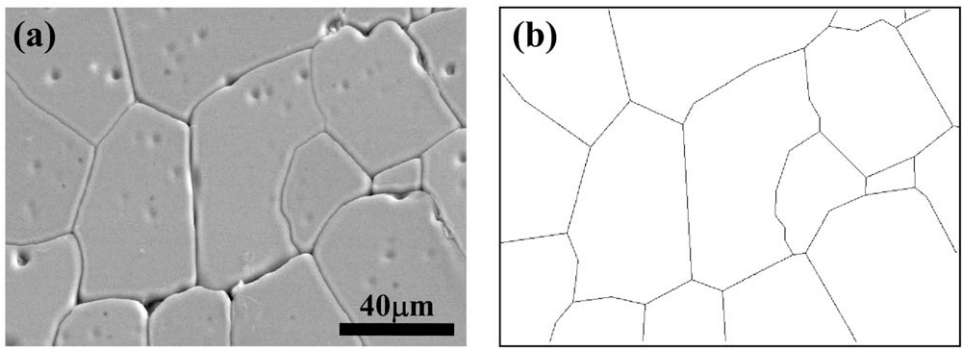


Fig. 1. (a) A typical grayscale SEM image after a correction for geometric distortions has been applied, and (b) the corresponding skeletonized image with the grain boundaries replaced by straight line segments.

neighbor pair [19]. However, when 196 images are positioned using only nearest neighbor offsets, cumulative errors arise. In other words, if the distance between two points in distant images is computed by summing the nearest neighbor offsets along two different paths through the array of images, the distances usually differ. So, the second step of the image positioning algorithm is to randomly select paths through the image array and reposition the images to minimize the differences between distances computed in the global reference frame and those determined by summing the nearest neighbor offsets along equivalent random paths. Positioning errors of less than one pixel were achieved with this method. Fig. 2a illustrates a montage created in this way.

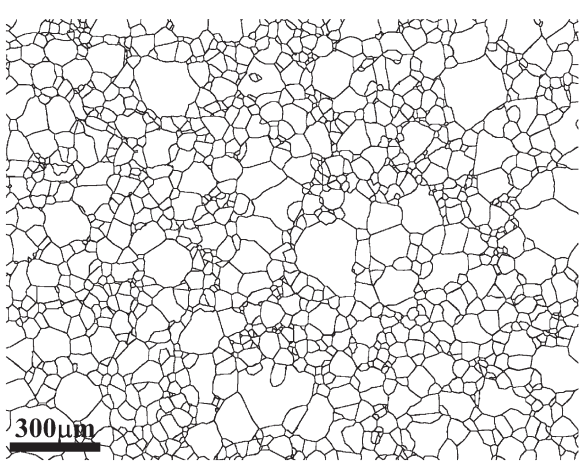


Fig. 2. A typical montage of skeletonized SEM images containing 196 individual images.

With the relative positions of each sector now established, the orientation data were combined with the skeletons to form high-resolution orientation maps. This was accomplished by first identifying every grain in a scan area by finding the contiguous pixels not associated with a grain boundary. Multiple orientation measurements were made in each grain and, typically, not all were consistent. To assign a single orientation, minority orientations resulting from errors in the indexing were excluded and the remaining majority orientations, which contained some scatter, were averaged [20,21].

Once the high-resolution orientation maps from each layer were obtained, it was necessary to align the maps to establish the same global reference frame for all five layers in a given column. The first layer was selected as the global reference frame. The transformation from all subsequent layers to the first layer is given by $\mathbf{Ax} + \mathbf{t}$, where $\mathbf{x}$ is a two-dimensional vector which represents the position within a given layer, A is a $2 \times 2$ affine transformation matrix, and $\mathbf{t}$ is a two-dimensional translation vector. To find $(A,\mathbf{t})$ for each layer, we initially find $(A,\mathbf{t})$ that maximizes the area of overlap between positions with the same orientations on adjacent layers by using a downhill simplex minimization routine [22]. Pixels on adjacent layers are considered to overlap if the orientations are within 5°. The $(A,\mathbf{t})$ describing the transformation that aligns adjacent layers is then used to calculate the $(A,\mathbf{t})$ that aligns each layer with the initial layer. Two overlapping skeletons in Fig. 3 illustrate the result of this procedure.

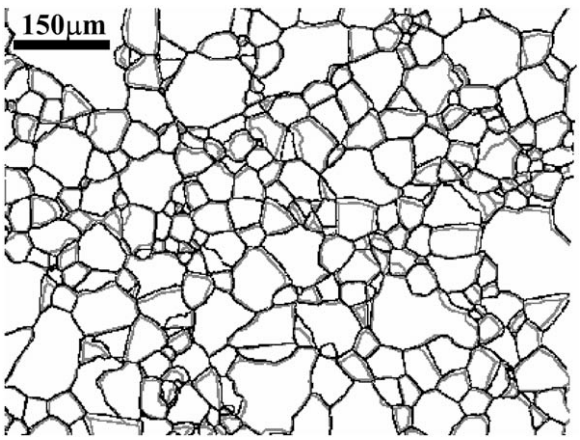


Fig. 3. A superposition of two skeleton image montages from adjacent layers in the microstructure after the alignment process.

After all layers were transformed into the global reference frame, it is necessary to identify sections from the same grain that appear in multiple layers. This is done by first determining the area of overlap between all grain section pairs on adjacent layers. The pair of grains that has the largest area of overlap is identified as being two sections of the same grain. The pair with the second largest area of overlap is then assigned in the same way. The process continues until all grains have been assigned or do not overlap any grains that have not been assigned. It was estimated that the algorithm successfully matches the correct grains on adjacent layers 99.5% of the time. The success of this algorithm derives from the fact that the distance between adjacent layers is much smaller than the average grain size. After the grain connectivity was established, the orientations of the crystallites were reassigned by repeating the process that was used in each layer, but now considering all of the orientation data from different section planes of the same grain.

From this three-dimensional reconstructed microstructure, we wish to determine the total observed area of each type of grain boundary. To identify individual plane segments with a specific type, a triangular mesh connecting the grain boundary skeletons on each layer was constructed. First, the pixel locations were smoothed by averaging with the neighboring pixel positions. Next, the pixels from common grain boundaries on adjacent layers were extracted from the orientation maps. These pixels were identified by comparing the two crystallites adjacent to the boundary on each layer. Using the triple junction locations as end-points, the grain boundary pixels from both layers were ordered in the same manner. To create the mesh, the pixel positions on the second layer were projected on to the plane of the first and every fourth pixel position on both layers was considered as a vertex of a triangular element. As illustrated schematically in Fig. 4, triangular elements were constructed from the vertices by first connecting one of the sets of triple junction locations. Next, the distance to the next vertex position for each layer

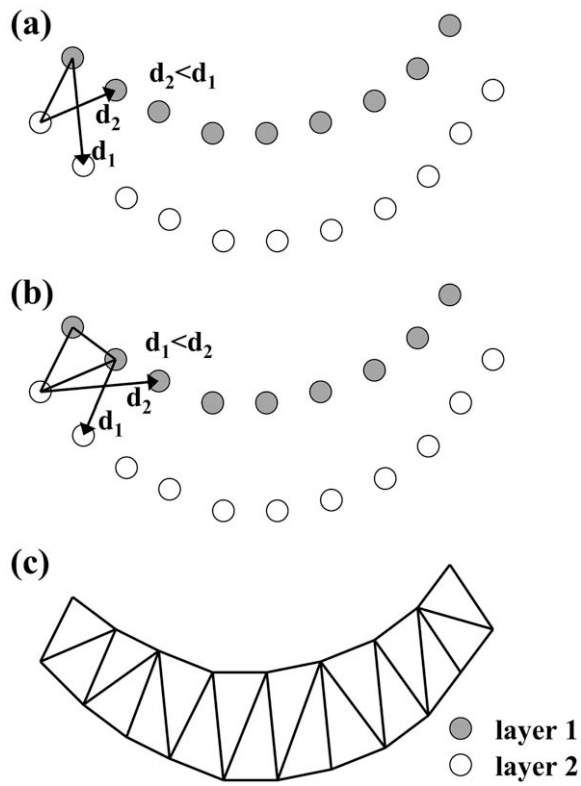


Fig. 4. (a) Illustration of the grain boundary meshing algorithm. First, the pixel positions on the second layer are projected on to the plane of the first layer. Next, the first set of triple junctions locations are connected, and the distance to the next vertex position for each layer ($d_i$) is calculated. (b) The vertex corresponding to the shortest distance is used to create the first element, and the process is repeated. (c) This continues until all pixels on both layers are connected.

was calculated. The vertex corresponding to the shortest distance was used to create the first element. For the next element, the last connected vertex on each layer was used and the shortest distance criterion was again applied to determine the third vertex. This process continued until the last pixel from both layers was connected. A total of $4.1 \times 10^6$ triangular mesh elements were used to represent all grain boundary surfaces in the characterized volume. For each mesh element, we can specify the area of the plane, the misorientation across the plane (from the measured orientations on either side of the boundary), and the normal to the plane. As described in the next section, this information allows us to specify the areal distribution of boundary types over the five macroscopic grain boundary parameters, $\lambda(\Delta g,\mathbf{n})$.

### 2.4. The grain boundary distribution

The measured orientations ($g_1$ and $g_2$) of adjoining crystals are used to calculate the misorientation ($\Delta g$) for each boundary plane. It is important to recognize that crystal symmetries lead to numerous values of $\Delta g$ that represent indistinguishable grain boundaries [2]. For an orientation of a cubic crystal, $g$, there are 24 equivalent $g$ given by $C_i g$, where $C_i$ ($i$ = 1 to 24) are the proper symmetry operators for cubic symmetry. Therefore, we can consider the misorientation with respect to the first grain, $\Delta g = C_i g_1 (C_j g_2)^T$, or with respect to the second grain $\Delta g = C_j g_2 (C_i g_1)^T$. This leads to $2 \times 24^2 = 1152$ equivalent misorientations. For each of these misorientations, we must also specify a boundary plane in one of the two crystal reference frames. For each $\Delta g$, we calculate the plane normal in the crystal reference frame ($\mathbf{n}$) using the measured planar normal in the sample frame ($\mathbf{n}'$) and the non-transposed reference frame. In other words, for the case of $\Delta g = C_i g_1 (C_j g_2)^T$, $\mathbf{n} = gC_1\mathbf{n}'$, and for the case of $\Delta g = C_j g_2 (C_i g_1)^T$, $\mathbf{n} = gC_2\mathbf{n}'$. Finally, we note that it is arbitrary whether the grain boundary normal points into first or second crystal. This adds an additional factor of two to the number of symmetrically equivalent boundaries, thus $2 \times 2 \times 24^2 = 2304$ symmetrically equivalent grain boundaries are generated from every observation.

We note that while the discussion above is complete for the vast majority of grain boundaries, there are bicrystal configurations that have additional symmetry that arises from symmetry about a common rotation axis and the interchange of the two crystals adjoining the boundary [23,24]. In this paper, we use only the minimal symmetry that applies to the general boundaries; the additional symmetries that occur in special cases arise naturally from our analysis and are apparent in the results. Since these special cases comprise a minority fraction of all possible boundaries, treating them separately does not provide a meaningful advantage in our analysis.

Three Eulerian angles ($\phi_1$,$\Phi$,$\phi_2$) are used to specify the misorientation ($\Delta g$) and two spherical angles, $\theta$ and $\phi$, are used specify the grain boundary plane normal ($\mathbf{n}$). The domain of misorientations was parameterized by $\phi_1$, $\cos(\Phi)$, and $\phi_2$ in the range of zero to $\pi/2$, 1, and $\pi/2$, respectively. The spherical angles were parameterized by $\cos(\theta)$ and $\phi$ in the range of zero to 1 and $2\pi$, respectively. This sub-domain, which is 1/64th of the entire range possibilities, is a convenient choice because it is the smallest volume that contains an integer number of fundamental zones and can still be partitioned in a simple way. Therefore, every observed grain boundary has 36 (=2304/64) symmetrically equivalent grain boundaries in the sub-domain. The choice of parameters allows the sub-domain to be partitioned in cells of equal volume when the parameters are equally partitioned. Here, $\Delta\phi_1 = \Delta\phi_2 = \Delta\phi = 90°/9$ and $\Delta\cos(\Phi) = \Delta\cos(\theta) = 1/9$. The cell size must be large enough so that most contain a statistically significant number of observations and small enough that textural features can be revealed. While there are $4.1 \times 10^6$ observed triangular mesh elements, many of these are indistiguishable observations, formed when a planar boundary is partitioned into smaller triangular mesh elements with the same parameters. Based on the number of distinct grains in the data set, we estimate that there are on average at least eight independent observations of each of the 6521 distinct types of boundaries. After the areas of all mesh elements have been summed in the appropriate cells, the area in each cell is normalized such that the average value is one. Thus, because the cells are of equal volume, the value in each cell,

$\lambda(\Delta g,\mathbf{n})$, is a multiple of a random distribution (MRD). For any specified type of grain boundary, the MRD value is determined by averaging the MRD values of the corresponding 36 symmetrically equivalent cells within the domain.

## 3. Results

The resulting grain boundary distribution function is five-dimensional and visual examination is challenging. We begin by examining separately the distribution of misorientations, $\lambda(\Delta g)$, averaged over all boundary planes (Fig. 5a), and the distribution of boundary planes, $\lambda(\mathbf{n})$, averaged over all misorientations (Fig. 5b). The results show that this sample has significant texture both in the space of misorientations and grain boundary planes. The distribution of grain boundaries averaged over all values of $\mathbf{n}$, $\lambda(\Delta g)$, is shown in Rodrigues–Frank space. Here, each $\Delta g$ is denoted by a unique vector with a direction parallel to the common axis of misorientation and a magnitude that is proportional to the tangent of one half of the misorientation angle. In Fig. 5a, the $\mathbf{r_1}$ direction is parallel to [100] and the nine individual plots show slices through the three dimensional space perpendicular to [001] ($\mathbf{r_3}$). In the misorientation distribution, there are strong peaks at low angle misorientations (~14 times random at maximum); for larger angles (>15°), misorientations about the [111] axis dominate the population; the axial texture about [111] is about 11 times random. The distribution of grain boundary planes (Fig. 5b) shows peaks at the {100} planes. Averaged over all of the observations, the planes occur with more than twice the random frequency.

At specific misorientations, the distribution of grain boundary planes exhibits more dramatic and complex variations. To illustrate these variations, a fixed misorientation specified by an axis–angle pair (for the purposes of viewing the five-dimensional space, this is more convenient than the Euler angle parameterization), and the distribution of boundary orientations is plotted on a stereographic projection. As an illustration, Fig. 6 shows the distribution of boundary planes for a 5° rotation about the [110] axis. In this projection, the misorientation axis lies in the plane of the paper. The boundaries with normals parallel to this axis are pure twist, while those that are perpendicular (those along the great circle from $[\bar{1}10]$, to [001], to $[1\bar{1}0]$ that is marked with a 't') are pure tilt boundaries. For this misorientation, we see that the tilt boundaries are favored over twist and that the peak of the distribution occurs for {110} tilt planes. There are also local maxima at the {100} positions.

Fig. 7 illustrates how the distribution of grain boundary planes changes with misorientation angle for boundaries with <100> misorientation axes. At each misorientation angle, a peak in the distribution occurs at a {100} type plane; this is consistent with the misorientation averaged data presented in Fig. 5b. While these are the only peaks in the distribution at relatively low angles (15°), the distribution broadens at higher angles (25°) and eventually multiple peaks emerge (35° and 45°). These changes are easy to understand if one considers the strong preference for {100} type planes and the geometric constraints associated with creating a bicrystal. For {100} twist boundaries, both crystals can be terminated by a {100} plane. Thus, we notice that the distribution of grain boundary planes around the twist positions, indicated with crossed circles on the stereographic projections, do not change significantly with misorientation angle. However, for pure tilt boundaries, if one of the terminating planes is fixed at {100}, the complementary plane in the adjoining crystal must have a different index. Therefore, we see that along the zone of pure tilt boundaries, the population varies systematically. When one crystal is terminated by (001), the complementary crystal must be terminated by a (0k1) plane inclined by the misorientation angle from (001). Thus, the peak at (001) spreads along the zone of the tilt boundaries as the misorientation angle increases and, at 35°, forms a separate peak inclined from (001) by this same angle. Excluding the maxima at {110} positions found at low misorientation angles, all of the peaks in the distribution can be accounted for by bicrystals in which at least one crystal is terminated by a {100} plane.

Fig. 8 shows the distribution of grain boundary planes at nine additional points in the high angle region of misorientation space. The projections in

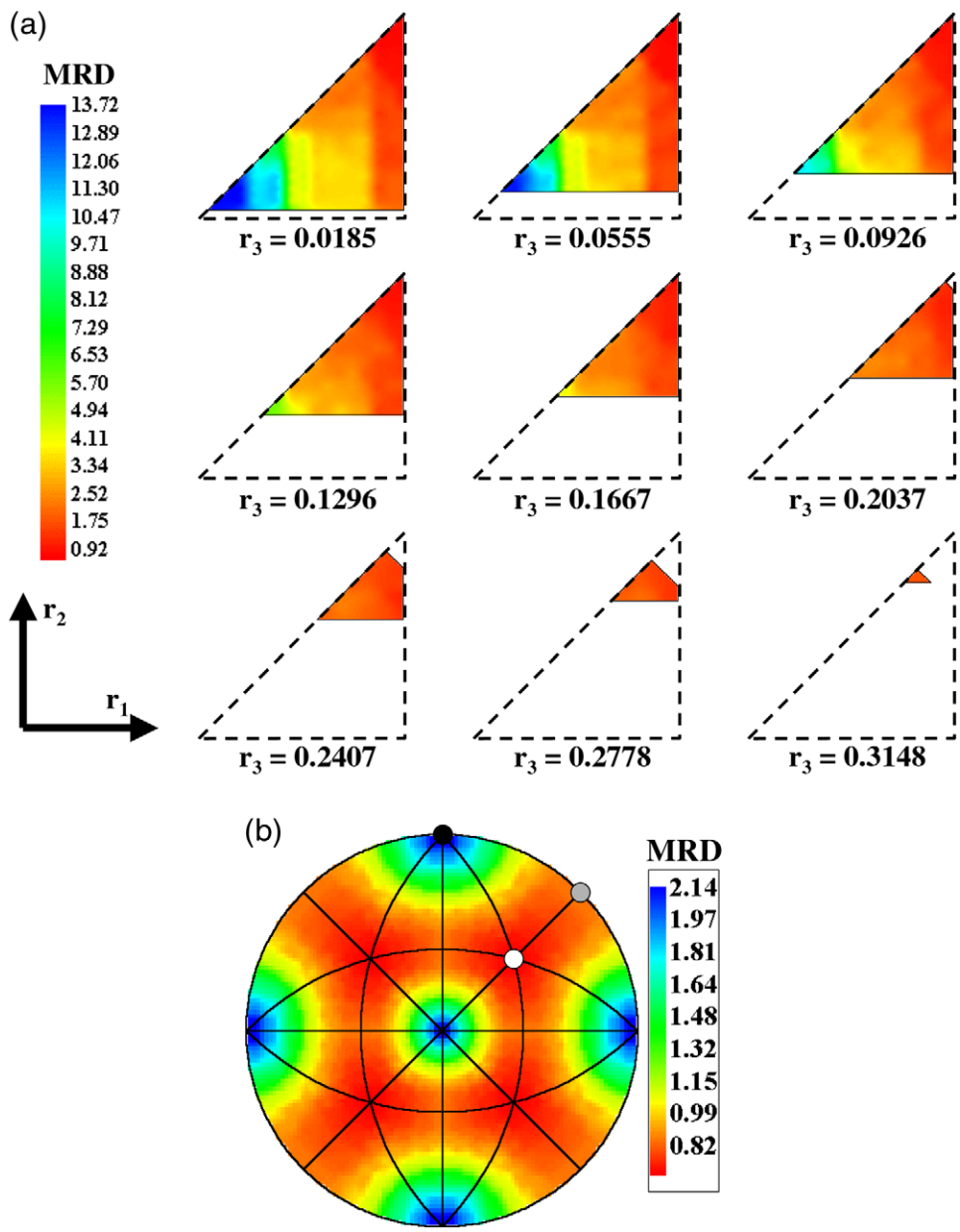


Fig. 5. Projections of the five-parameter grain boundary distribution. (a) The three-dimensional distribution of misorientations, parameterized as Rodrigues vectors, averaged over all boundary planes. The plot shows progressive slices through the asymmetric domain for cubic misorientations along the $r_3$ axis. (b) The misorientation averaged distribution of boundary planes plotted in stereographic projection, with the (010), (110) and (111) planes marked with a solid black, gray and white circle, respectively.

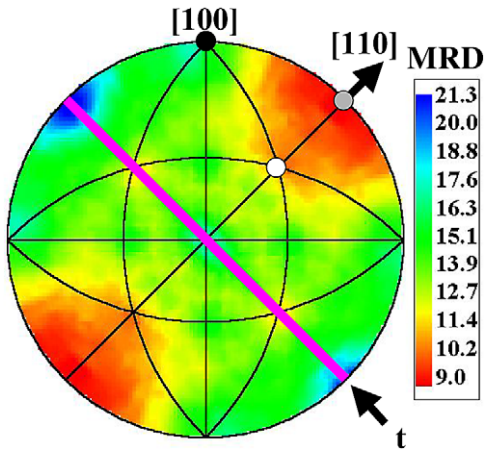


Fig. 6. The observed distribution of grain boundary planes for a 5° misorientation around [110]. The populations, which are normalized and represented as multiples of a random distribution, are plotted in stereographic projection. The directions that correspond to pure tilt boundaries are also indicated (t).

Fig. 8a–c show the distribution of plane at 20°, 40° and 60 ° about <110>. Data for the same rotation angles about the <111> and <952> axes are included in Fig. 8d–f and Fig. 8g–i, respectively. Note that the boundaries with <110> and <111> misorientations, like those with <100> misorientations, have special symmetries arising from their misorientation axes. The [952] axis, on the other hand, lies at the center of the standard stereographic triangle and these misorientations are included as representatives of truly general boundaries that have only the symmetry associated with the reversal of the boundary normal direction. The one common feature of these distributions is that every one includes maxima at {100} planes. At 20°, the peaks are centered very near the {100} positions. As was the case for the boundaries with <100> type misorientations, these peaks broaden with misorientation angle and at higher angles, new peaks arise. In each case, the new peaks are associated with the geometrically necessary complement to a {100} plane. The tendency of the grain boundary to lie parallel to a {100} means that grain boundaries in magnesia also tend to be asymmetric.

## 4. Discussion

Serial sectioning preferentially reveals grain boundary planes that are perpendicular to the analysis surface. Since the sample had strong axial <111> texture, planes in the <111> zone should intersect the plane of analysis more frequently than others. Since this zone does not include {100}, the high observed population grain boundaries with the {100} planes is not an artifact of the experimental geometry and the grain orientation texture. However, the sample geometry and texture does limit our ability to observe certain types of grain boundaries. Since the majority of the grains are oriented so that <111> is perpendicular to the plane of analysis, the observation of <111> type twist boundaries is unlikely. This limitation is easily confirmed by the data; note that Fig. 8d–f, showing the distribution of planes for boundaries with <111> misorientation axes, display minima at pure twist positions. Since this minimum is likely to be an artifact of the experimental geometry, it is not possible to conclude anything about the relative population of grain boundaries at these particular points in the five-dimensional space, which includes the coherent twin.

To demonstrate that the observed trends are robust with respect to the size of the cells, we have also calculated the distribution using a finer discretization. In this case, the subdomain of the grain boundary parameters was partitioned into cells with $\Delta\phi_1 = \Delta\phi_2 = \Delta\phi = 90°/12 = 7.5°$, and $\Delta\cos(\Phi) = \Delta\cos(\theta) = 1/12$ (compared to 1/9 for the previous analysis). While the maximum and minimum of the distribution change (28.8 and 0.0, respectively, for the finer partitioning, compared to 22.0 and 0.0 obtained using the larger cells), the trends were similar to those in the distribution calculated using the coarser partitioning. To quantify this similarity, we have used the Spearman [22] rank-order correlation coefficient ($r_s$), which ranges from −1 to 1 to indicate perfect negative and positive correlations, respectively; for $r_s = 0$, no correlation exists. Comparing the distribution of boundary configurations calculated from the coarse and fine distributions, we find that $r_s = 0.94$; this indicates a very strong correlation between the two distributions. In general, coarser partitions are

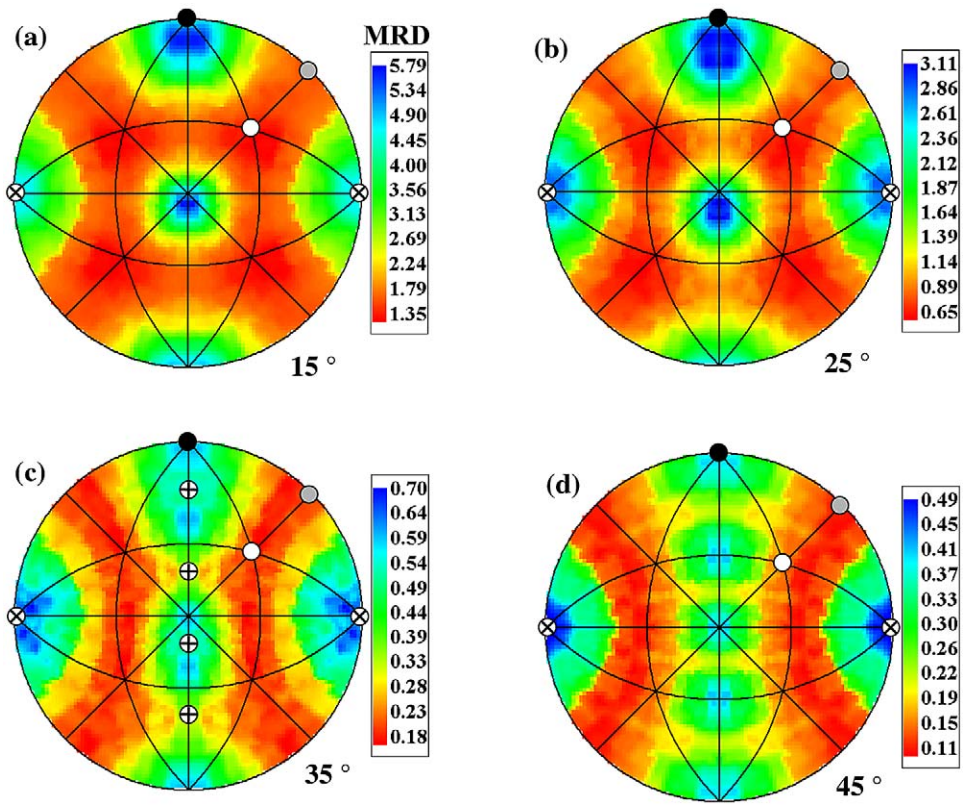


Fig. 7. The observed distribution of grain boundary plane normals for boundaries with misorientations of (a) 15°, (b) 25 °, (c) 35° and (d) 45° around the [100] axis. The populations, which are normalized and represented as multiples of a random distribution, are plotted in stereographic projection. Also, the pure twist and symmetric tilt boundaries are indicated with a circled x and +, respectively.

expected to lead to a greater smoothing of the data. Since the resolution of the grain boundary plane orientations, which is limited by the serial sectioning process, is estimated to be no better than 7.5°, finer partitions are not meaningful.

To demonstrate the observed trends are robust with respect to the scheme used to partition the five-dimensional space, we have also repeated the calculation using cells that all span the same angular range (10° in all parameters). We refer to this as 'equal angle' parameterization. When $\lambda(\Delta g,\mathbf{n})$ is computed using the equal angle parameterization, it spans a larger range of MRD values; the maximum and minimum are 27.1 and 0.0, respectively. However, a visual inspection of the distribution indicates that the trends are similar. Comparing the distribution of boundary configurations from the two different discretizations, we find $r_s$ = 0.97, which again indicates a very strong correlation [25]. Therefore, the results are not strongly dependent on the method used to partition the five-dimensional space.

It should be recognized that when the grain boundary distribution is presented in the axis–angle space, the low misorientation angle boundaries are more affected by the size of the cells than the high misorientation angle boundaries. The discrete cells in the sub-domain of boundary space that correspond to misorientations of less than approximately 10° contain all possible misorientation axes. Therefore, the distribution of boundary planes for any fixed low angle misorientation is generated from approximately the same cells. However, a separate examination of these boundaries shows that the <110> misorientation axes are by far the most common. Therefore, even

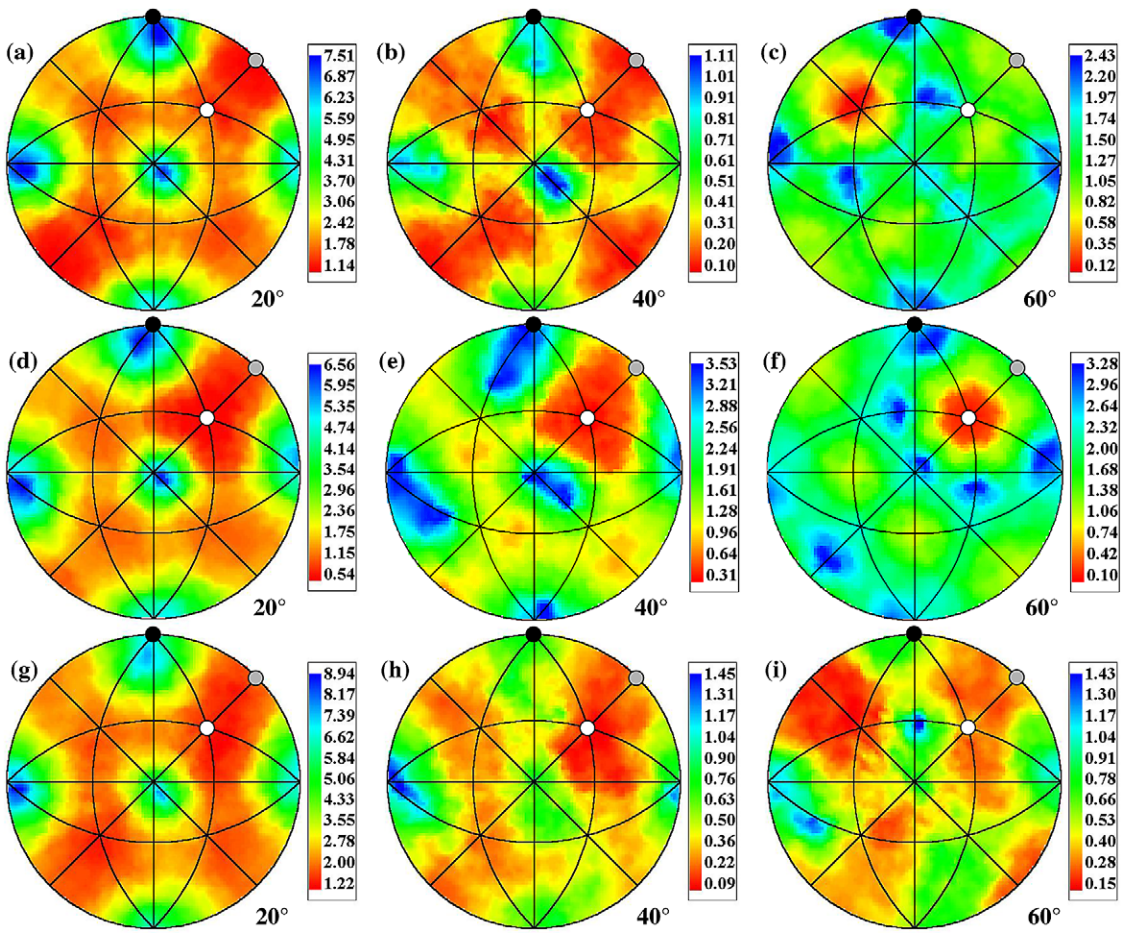


Fig. 8. The observed distribution of grain boundary plane normals for boundaries with misorientations corresponding to rotations about [110] of (a) 20°, (b) 40° and (c) 60°, rotations about [111] of (d) 20°, (e) 40° and (f) 60°, and rotations about [952] of (g) 20°, (h) 40° and (i) 60°. The populations, which are normalized and represented as multiples of a random distribution, are plotted in stereographic projection.

though the projection shown in Fig. 6 averages data over a range of misorientation axes, the dominant contribution is from <110> boundaries and it is therefore thought to be an adequate representation of the grain boundary plane distribution for low angle misorientations about <110>.

For the case of a general bicrystal, the unique zone of boundary planes for a general fixed misorientation is a hemisphere ($0 \leq \theta < \pi/2$, $0 < \phi < 2\pi$). However, in cases where the two crystals share an axis of rotational symmetry, the bicrystal has additional symmetry that results from combining the rotational symmetry of the common axis with operations that relate positions in the two crystals without regard for the crystal of origin [23,24]. If the common axis has n-fold rotational symmetry, then the range of unique planes is reduced such that $0 \leq \omega \leq \pi/n$, where $\omega$ is defined as the azimuthal angle about the axis of symmetry originating at a symmetric tilt boundary (the polar angle $\theta$, away from the direction of the symmetry axis, remains in the range of $0 \leq \theta \leq \pi/2$). An example of this symmetry can be seen in Fig. 7c which shows the distribution of boundary planes for a fixed misorientation of 35° about <100>. Since the crystals share a <100> axis, the highest

common shared symmetry element is 4/m and this reduces the range of unique planes to $0 \leq \omega \leq \pi/4$. Therefore, a zone of unique planes includes all orientations between the <100> twist and two symmetric tilts, which are shown on the plot. For all of the special cases examined, the expected bicrystal symmetries arose naturally from an independent consideration of the symmetries of each component crystal.

The results for the sample examined here show a strong texture in the space of grain boundary planes. Since there are no previous detailed studies of grain boundary distributions as a function of all five parameters, it is not yet known if this type of texture occurs in other crystalline materials. Since grain boundary energy anisotropy is the most likely source of the grain boundary plane texture, we expect the phenomenon to occur in any materials whose grain boundary energies are anisotropic. The variation of the grain boundary free energy over the macroscopic parameters, and the possibility that this is the source of the observed grain boundary plane texture, are discussed in detail in the companion paper [14].

## 5. Summary

We have measured the five macroscopic parameters of more than one million boundary plane segments making up 5.4 $mm^2$ of grain boundary interface area in a hot-pressed magnesia polycrystal. Using these data, it is possible to examine the crystallographic texture of the grain boundary planes. For grain boundaries at low misorientation angles, there is a preference for tilt boundaries, especially those with boundary plane normals in the <110> direction. For all misorientations greater than 10°, the results show that grain boundary planes in magnesia most frequently adopt asymmetric configurations in which the interface is parallel to the {100} plane in one of the two crystals. Grain boundaries terminated on a {100} plane occur with twice the frequency of other types of grain boundaries.

## Acknowledgements

This work was supported primarily by the MRSEC program of the National Science Foundation under Award Number DMR-0079996.

## References

[1] Goux C. Can Metall Q 1974;13:9.
[2] Morawiec A. Symmetries of grain boundary distributions. In: Weiland H, Adams BL, Rollett AD, editors. Proceedings of the Third International Conference on Grain Growth. Warrendale, PA: TMS; 1998. p. 509–14.
[3] Saylor DM, Morawiec A, Adams BL, Rohrer GS. Interface Science 2000;8:131.
[4] Pospiech J, Sztwiertnia K, Haessner F. Textures Microstruct 1986;6:201.
[5] Heidelbach F, Wenk HR, Chen SR, Pospiech J, Wright SI. Mater Sci Engng A 1996;A215:39.
[6] Williams WM, Smith CS. J Metals 1952;194:755.
[7] Alkemper J, Voorhees PW. Acta Mater 2001;49:897.
[8] Randle V, Davies H. Ultramicroscopy 2002;90:153.
[9] Duyster J, Stöckhert B. Contrib Mineral Petrol 2001;140:567.
[10] Krakauer BW, Seidman DN. Interface Science 2000;8:27.
[11] Poulsen HF, Nielsen SF, Lauridsen EM, Schmidt S, Suter RM, Lienert U, Margulies L, Lorentzen T, Juul Jensen D. J Appl Cryst 2001;34:751.
[12] Adams BL, Wright SI, Kunze K. Met Trans A 1993;24:819.
[13] Saylor DM, Morawiec A, Rohrer GS. J Amer Ceram Soc 2002;85:3081.
[14] Saylor DM, Morawiec A, Rohrer GS. Acta Mater 2003. doi:10.1016/S1359-6454(03)00182-4.
[15] Saylor DM, Mason DE, Rohrer GS. J Amer Ceram Soc 2000;83:1226.
[16] Morawiec A. J Appl Cryst 1999;32:788.
[17] Bunge H-J. Texture analysis in materials science. London, UK: Butterworths, 1982 p. 21, translated by P.R. Morris.
[18] Kapur J, Casasent D. Proceedings SPIE 2000;4044:165.
[19] Mahadevan S, Casasent D. In: Proceedings SPIE 2001;4387:204.
[20] Morawiec A. J Appl Cryst 1998;31:818.
[21] Humbert M, Gey N, Muller J, Esling C. J Appl Cryst 1996;29:662.
[22] Press WH, Flannery BP, Teukolsky SA, Vetterling WT. Numerical recipes in pascal. Cambridge, UK: Cambridge University Press, 1989.
[23] Pond RC, Bollman W. Roy Soc London Phil Trans 1979;292:449.
[24] Kalonji G, Cahn JW. J de Physique 1982;43:C6–25.
[25] Williams F. Reasoning with statistics. Fort Worth: Harcourt Brace Jovanovich, 1992.